



Article

Testbed for Multilayer Conformal Additive Manufacturing

Michael D. M. Kutzer * and Levi D. DeVries

Weapons & Systems Engineering, United States Naval Academy, 105 Maryland Avenue, Annapolis, MD 21402, USA; devries@usna.edu

* Correspondence: kutzer@usna.edu; Tel.: +1-410-293-6113

Academic Editors: Salvatore Brischetto, Paolo Maggiore and Carlo Giovanni Ferro

Received: 8 April 2017; Accepted: 19 May 2017; Published: 24 May 2017

Abstract: Over the last two decades, additive manufacturing (AM) or 3D printing technologies have become pervasive in both the public and private sectors. Despite this growth, there has been little to no deviation from the fundamental approach of building parts using planar layers. This undue reliance on a flat build surface limits part geometry and performance. To address these limitations, a new method of applying material onto or around existing surfaces with multilayer, thick features will be explored. Prior work proposes algorithms for defining conformal layers between existing and desired surfaces, however this work does not address the derivation of deposition paths, trajectories, or required hardware to achieve this new type of deposition. This paper presents (1) the derivation of deposition paths given a prescribed set of layers; (2) the design, characterization, and control of a proof-of-concept testbed; and (3) the derivation and application of time evolving trajectories subject to the material deposition constraints and mechanical constraints of the testbed. Derivations are presented in a general context with examples extending beyond the proposed testbed. Results show the feasibility of conformal material deposition (i.e., onto and around existing surfaces) with multilayer, thick features.

Keywords: additive manufacturing; articulated robotics; coordinated manipulation; coordinated trajectory planning; manipulator control

1. Introduction

In a 2015 briefing on AM technologies [1], it was reported that the Naval Systems Engineering Directorate (NAVSEA 05) currently supports upwards of 130 pieces of AM equipment enabling more than a half dozen printing methodologies in materials ranging from ABS plastics to 17-4 PH steel. This equipment is primarily used for research, design, and prototyping applications; however the vision of NAVSEA 05 is to operationalize AM technology in direct support of the fleet with the stated goal of “establish[ing] the processes, specifications and standards for use of AM for ship acquisition, design, maintenance, and operational support [1]”. Five years earlier, the Chief Scientist of the Air Vehicle Engineering Department within the Naval Air Systems Command (NAVAIR) [2] identified metallic AM as having the potential “to enhance operational readiness, reduce total-ownership-cost, reduce energy consumption, and enable parts-on-demand manufacturing”. In April 2015, NAVAIR reported plans to introduce a flight-critical metal component produced using metallic AM by November of 2017 [3].

Additive manufacturing (AM) or 3D printing technology leverages a variety of processes to bind materials, creating solid structures. AM fabrication offers relaxed design rules and simple part-by-part customization. Unlike part fabrication using subtractive machining, inexperienced developers can produce physical hardware almost immediately with AM; while experienced designers can create complex parts tailored for specific applications. In the context of defense logistics, AM has the capability

of “truncating the entire [supply] process and meeting the need exactly where it is [4]”. The AM production of certified, field-ready hardware can move the entire supply chain forward to the point of need. This capability can also completely eliminate the need for stockpiled parts, as replacements can be stored electronically and produced on demand. Table 1 summarizes current commercial AM technologies by process (processes are defined using the ASTM F2792 12a Standard Terminology for Additive Manufacturing Technologies).

Table 1. Summary of Commercial AM Technologies [5].

Process	Description	Material(s)
Binder Jetting	A liquid bonding agent is selectively deposited to join powder materials	Polymers, Sand, Glass, Metals
Direct Energy Deposition	Focused thermal energy is used to fuse materials by melting as they are deposited	Metals
Material Extrusion	Material is selectively dispensed through a nozzle or orifice	Polymers
Material Jetting	Droplets of build material are selectively deposited	Polymers, Waxes
Powder Bed Fusion	Thermal energy selectively fuses regions of a powder bed	Metals, Polymers
Sheet Lamination	Sheets of material are bonded to form an object	Paper, Metals
Vat Photopolymerization	Liquid photopolymer in a vat is selectively cured by light-activated polymer	Photopolymers

In AM processes, parts are made by iteratively adding layers of material. Each layer is defined by a thin cross-section of a 3D part exported from a computer-aided design (CAD) model [6]. In general, commercial AM systems use a “build-bed” that serves as the flat substrate for part fabrication. The CAD model is imported into an AM software package, and positioned/oriented relative to the build-bed. Layers are then defined by equally spaced planar slices of the CAD model, parallel to the build-bed. This layering approach is effective for a wide variety of part geometries, however issues may arise with overhanging features. These issues are generally avoided by adding sacrificial support material that is removed following the completion of the AM process [6]. Use of support material (also known as support structure) is common practice in material extrusion, material jetting, and powder bed fusion processes. Although effective, this approach wastes material and adds to the fabrication time. Extensions of the work presented in this paper may reduce the need for support material by coordinating the position and orientation of both the build-bed and print-head.

In this paper, we derive deposition trajectories by coordinating the position and orientation of both the tool-head and build-bed. Similar research has explored the concept of conformal printing onto non-planar surfaces (i.e., surfaces not adhering to the constraints of a plane in Euclidean space) for a variety of applications including subtractive processes like lithography used to produce optics [7,8], and additive methods to fabricate antennas and electronics onto/into mechanical components [9,10]. In general, the AM techniques explored for conformal applications involve “direct write” technologies [6] used to produce thin features on surfaces. One primary exception is the work of Davis et al. [5] that explores algorithms for deriving layers between surfaces, but does not address the transition from layering to material deposition. Related metal deposition methods involve using directed energy and welding to extend printing capabilities by increasing the total degrees of freedom (DOF) or axes used to drive the nozzle or AM tool-head. Unlike the traditional three axis Cartesian (i.e., x , y , and z) stages used by common AM methods like fused deposition modeling (FDM); directed energy deposition (DED) approaches often use four or five axes to drive the relative position between the AM tool-head and build surface (Loughborough University [11]), however deposition generally takes place on a flat or near-flat build-bed.

Conformal AM with multilayer, thick features can be achieved using the layering algorithms presented in [5] in conjunction with registration and manipulation methods commonly used in robotics. This paper replaces the concept of a build-bed with a largely arbitrary “build-object” referring to an application substrate with arbitrary geometry. AM material is directly deposited onto a build-object and layered, adding features to existing surfaces or completely encapsulating the build-object (i.e., applying material to/around an existing part). With sufficient articulation of the build-object, the need for support material commonly used in extrusion-based systems (e.g., FDM) beneath overhanging surfaces [6] may be reduced or eliminated by actively reorienting the deposition path relative to gravity. Doing so may reduce printing time, reduce wasted material, and further reduce design constraints; permitting features such as large sealed cavities. This paper focuses on the derivation of coordinated trajectories for the tool-head and build-object to create prescribed layer geometries. Given the level of articulation redundancy in the proposed system, actively reorienting the deposition direction and build-object orientation relative to gravity to eliminate the need for support material may be attainable but is outside the scope of this work.

While the complexity to implement conformal AM will vary largely with the AM technique, the underlying approach will remain consistent. Assuming the desired (final) part geometry is provided (i.e., produced by a designer in CAD software); this approach requires the following steps:

1. Identify and fixture the build-object,
2. Create (e.g., using 3D scanning) or import a surface model of the build object,
3. Register build-object to a common reference frame,
4. Register desired (designed) part geometry to a common reference frame,
5. Generate the build layers,
6. Generate the tool-head path relative to the build-object adhering to prescribed deposition and system constraints,
7. Generate the tool-head trajectory relative to the build-object adhering to prescribed deposition and system constraints,
8. Generate the build-object and tool-head trajectories adhering to deposition and system constraints, and
9. Build the part.

The distinction between a “path” and “trajectory” in these steps highlights the distinction between positions and orientations purely in space (i.e., oriented points along a path) and positions and orientations evolving in time (i.e., oriented points along a trajectory). This distinction is critical for deposition methods as time dependence is dictated by the details of deposition (e.g., material feed rate and thermal considerations).

Execution of this new AM process requires, at a minimum, articulation of the build-object relative to the AM tool-head used to deposit material. Depending on build-object geometries, this procedure may further benefit from additional articulation of the AM tool-head to sufficiently reach and deposit material per the model specification. The fundamental dual manipulator concept explored in this work is shown in Figure 1. In this concept, industrial-style manipulators are used in coordination to move both the build-object and AM tool-head. This redundant approach expands the manipulation space of the system by providing several benefits including compensation for potential interference issues between the build-object and AM tool-head.

In this context, the combined system contains ≥ 12 DOF to command the coordinated trajectories of the manipulators (assuming each industrial manipulator contains six or more joints). The mapping that relates the relative trajectory for material deposition (prescribed in 6-DOF) to the coordinated trajectories of the manipulators is underdetermined. This provides flexibility as there may exist multiple (potentially infinite) sets of coordinated manipulator trajectories that produce the same relative trajectory for material deposition. This flexibility enables coordinated trajectories to be selected to eliminate interferences/collisions, enable the application of additional constraints on deposition (e.g., reorienting the part to reduce/eliminate support structure), etc.

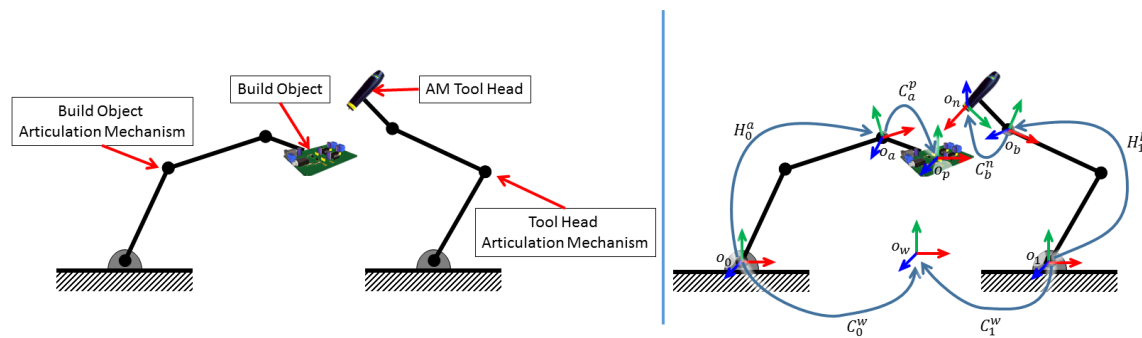


Figure 1. Illustration of fully articulated build-object and tool-head (**left**), and example coordinate frame assignments with associated transformation definitions (**right**) highlighting the minimum position/orientation measurements required to achieve conformal AM with this approach.

This paper presents the fundamental methods required to demonstrate conformal additive manufacturing. The methods presented include (1) the derivation of deposition paths given a prescribed set of layers; (2) the design, characterization, and control of a proof-of-concept testbed; and (3) the derivation and application of time evolving trajectories subject to the material deposition constraints and mechanical constraints of the testbed. Derivations are presented in a general context with examples extending beyond the proposed testbed. Results show the feasibility of conformal material deposition (i.e., onto and around existing surfaces) with multilayer, thick features.

Section 2 provides a summary of layering methods as applied to this approach using the prior work of Davis et al. [5]. Section 3 presents a new approach to defining paths for filling layers leveraging a projected ring approach as opposed to more common methods inspired by space filling curves [12]. Section 4 derives a general method to create coordinated deposition trajectories assuming manipulation of both the build-object and tool-head. Trajectory constraints are prescribed in the context of physical system limitations (e.g., velocity and acceleration constraints) and a simplified set of deposition constraints common to FDM methods. Section 5 reviews the system testbed design, associated geometric constraints, and coordinated control and provides a specific application example of deposition trajectory derivation based on the constraints of the testbed. Section 6 reviews the calibration of the system and summarizes experimental tests.

2. Review of Layering Methods

Davis et al. [5] present two approaches for defining conformal layers between two co-registered surfaces (the build-object and desired object geometry). The first method involves the use of a variable offset curve $\vec{x}_1(t; r)$ resulting from a parametrized curve $\vec{x}_0(t)$ as defined

$$\vec{x}_1(t; r) = \vec{x}_0(t) + r(t)\hat{N}(t). \quad (1)$$

Here, $r(t) \in \mathbb{R}^+$ is a parametrically-varying scalar and $\hat{N}(t)$ is the unit normal to $\vec{x}_0(t)$. For this method to be applicable, [5] assumes (1) the build-object is a convex geometry; (2) the desired object geometry is at most star-convex; and (3) the build object centroid is positioned relative to the desired part centroid to ensure intersections of the unit normal.

For the 2D case, two curves are given, γ_0 and γ_1 where $\gamma_0 \subset \gamma_1$. Here, γ_0 represents the 2D surface of the build object, and γ_1 represents the 2D surface of the desired part. For example, Figure 2 (left) illustrates a circular curve γ_0 and elliptic γ_1 . For generality, curves are represented by piecewise parametric cubic splines fit to two sets of ordered points. Normals to γ_0 are defined at regular intervals, and intersections between these normals and γ_1 are calculated. Normal segments are then length parametrized, and variable offset curves can be defined using points along the parametrized normals.

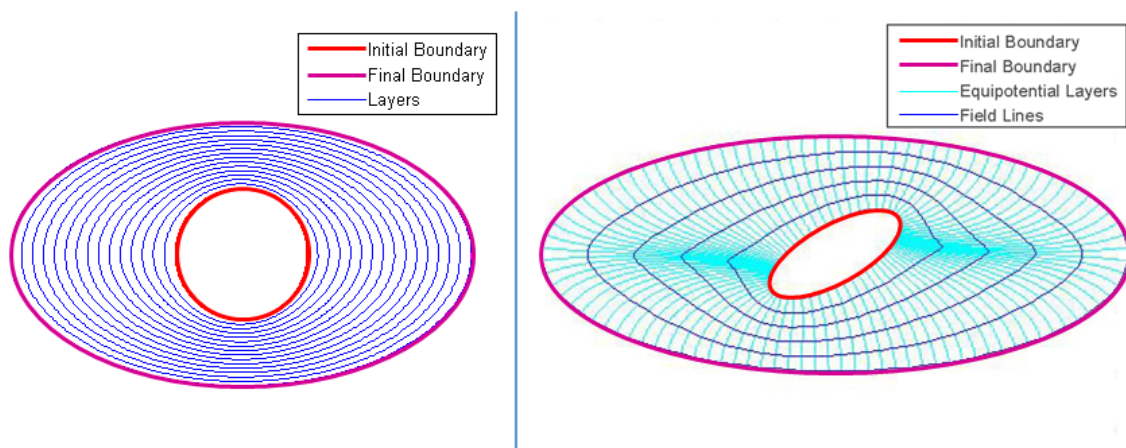


Figure 2. Variable offset curves derived between a build-object defined by a circle and desired object geometry defined by an ellipse (**left**); and Equipotential curves derived from solutions to Equation (2) (**right**).

Extending the concept of a variable offset curve into 3D to define variable offset surfaces is accomplished in a similar fashion to the approach taken for 2D. While the offset curves (or layers) produced appear evenly distributed, the algorithm is only applicable to a small subset of shapes.

To address non-convex geometries, [5] provide an alternate approach leveraging solutions to Laplace's equation for defining layers between curves. For an electrostatic potential field defined by $\varphi(x, y, z)$, Laplace's equation is given by

$$\nabla^2 \varphi = \left(\frac{\partial^2}{\partial x^2} + \frac{\partial^2}{\partial y^2} + \frac{\partial^2}{\partial z^2} \right) \varphi(x, y, z) = 0 \quad (2)$$

and solved by applying boundary conditions. For this application, boundary conditions are defined by the surfaces of the build-object and desired part, and layers are defined as equipotential surfaces in the simulated electric field around the build-object. Figure 2 (right) illustrates a simple 2D example.

This method is well suited for arbitrary geometries and can be extended from simple shape examples in 2D to application relevant 3D geometries. Figure 3 shows the application of the Laplace approach to derive layers between a build-object defined as a populated circuit board, and a desired surface defined as a computer mouse.



Figure 3. Build-object defined as a 3D CAD model of a populated circuit board (left) and desired surface defined as 3D CAD model of a computer mouse. A cross-section of equipotential curves derived from solutions to (2) equation between the build-object and desired surface is shown in the center.

Both methods are further expanded to incorporate hollow-features (subject to geometric limitations) into the layering geometry. This allows layers to be defined both around the build-object and specified voids defined for weight reduction, material savings, etc. These layering methods will serve as the foundation for the approach presented in this paper.

It is of note that limitations still must be addressed before these methods can be generally applied; several of which are described in [5]. In addition to the limitations discussed in [5], issues of layer "smoothness" and the uniformity of layer spacing are currently unaddressed. As can be seen in Figure 2 (right), areas associated with dense field lines produce layers with apparent protrusions

that diminish closer to the exterior surface. While these layers are spaced “appropriately” under the constraints of [5], the layer geometry may prove difficult to realize in the deposition process. Similarly, inspection of Figures 2 and 3 suggests that the spacing between layers is not uniform at all points along a given layer surface. This implies that a single deposition pass may not sufficiently fill the space between the layers defined using the methods of [5].

3. Deposition Path Generation

Path or “scanning path” generation for existing AM systems is typically based on one or more space filling curve(s) where each discrete, flat layer is decomposed (typically relative to the outer surface of the part) and filled with material subject to prescribed infill constraints [12,13]. This approach has been extensively explored and applied across a wide variety of AM processes. For non-planar layers as proposed in this work, extensions of planar space filling curve approaches to non-planar layers is certainly feasible. As an example, any surface can be decomposed into a discrete set of open surfaces (e.g., cubed-sphere [14]), each discrete surface can then be mapped to a plane, and a desired space filling curve can be applied. Based on the “flatness” of each discrete surface, some additional steps may be necessary to maintain appropriate spacing between paths when mapped back to the non-planar surface.

For the FDM-based testbed considered in this work, we will explore an alternative approach inspired by the potential for layers defined by closed surfaces where it may be desirable to minimize unnecessary seams. Seams, in the context of FDM, are locations where a “material extrusion tool-path starts and ends on each closed part curve [15]”. In the context of existing FDM processes, seams are only considered on the outer surface of the part and should typically occur once per layer. Using this definition, seams are effectively concealed by defining the start and end positions of the outer path within the part [16].

In the context of conformal AM, we will consider the total number of seams for every layer wherein a seam is defined as a point where a new deposition path begins or ends. Using a decomposition approach discussed above, the level of surface discretization will be proportional to one half of the total number of seams (assuming each discrete surface includes a tool-path start and end position that do not coincide). As a result, decomposing each layer into a discrete set of open surfaces provides a suboptimal solution. As an alternative, we consider an approach that, under ideal conditions, provides one contiguous path for layer geometries.

For the purposes of demonstration and without loss of generality, consider an ellipsoid defined parametrically about a body-fixed coordinate frame located at the centroid and aligned with the principal axes

$$\begin{aligned}x_1(u, v) &= c_1 \cos(u) \sin(v) \\x_2(u, v) &= c_2 \sin(u) \sin(v) \\x_3(v) &= c_3 \cos(v).\end{aligned}\tag{3}$$

Here, c_1 , c_2 , and c_3 define the magnitude of the principal axes; x_1 , x_2 , and x_3 define coordinates referenced to a body-fixed frame aligned with the principal axes (defined \hat{x}_1 , \hat{x}_2 , and \hat{x}_3) and located at the volumetric center; u is constrained to $u \in [0, 2\pi)$; and v is constrained to $v \in [0, \pi]$ as shown in Figure 4. To define paths, we consider a series of concentric “rings” offset along any given principal axis $\hat{x}_k \forall k \in \{1, 2, 3\}$. Use of the principal axes to define rings is independent of the parametrization. This provides a method suitable for any smooth, C^1 continuous surface. Without loss of generality, we assume that $k = 3$ given the parametrization provided in Equation (3). As a result, the ring for a given $x_3(v_i) = c_3 \cos(v_i)$ is defined using

$$\begin{aligned}x_1(u, v_i) &= c_1 \cos(u) \sin(v_i) \\x_2(u, v_i) &= c_2 \sin(u) \sin(v_i),\end{aligned}\tag{4}$$

where $i \in \{0, 1, 2, \dots, i_{max}\}$ denotes the discrete ring, $u \in [0, 2\pi)$, $v_i \in [0, \pi]$, and v_0 can be assumed to be zero.

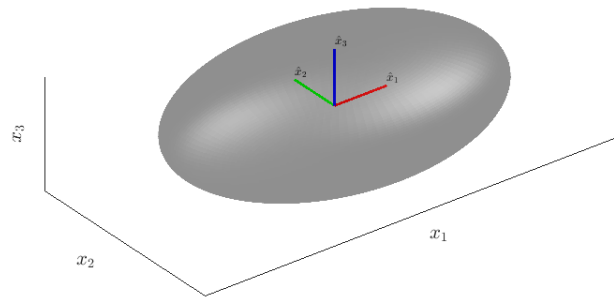


Figure 4. Ellipsoid with body-fixed coordinate frame located at the centroid and aligned with the principal axes \hat{x}_1 , \hat{x}_2 , and \hat{x}_3 .

Spacing between concentric rings is defined by the effective width of deposited material. Assuming material is deposited with a fixed circular cross section of radius r , v_i is calculated based on the previous ring v_{i-1} subject to the constraint

$$\left| (x_1(u, v_i) - x_1(u, v_{i-1}), x_2(u, v_i) - x_2(u, v_{i-1}), x_3(u, v_i) - x_3(u, v_{i-1}))^\top \right| = 2r. \quad (5)$$

As is expected for all but the special case where $c_1 = c_2$, this approach yields a problematic result as $i \rightarrow i_{max}$ where trajectory begins to self-intersect. Results for the $c_1 = c_2$ case are presented in Figure 5 and general results are shown in Figure 6.

The condition of a self-intersecting trajectory for a given ring i is described by

$$\left| \left((x_1(u, v_i), x_2(u, v_i), x_3(u, v_i))^\top \Big|_{u=u_{i,p}^*} - (x_1(u, v_i), x_2(u, v_i), x_3(u, v_i))^\top \right) \right| = 2r. \quad (6)$$

If and when this condition occurs, the ideal solution of two seams per layer must be relaxed. In the case shown in Figure 5, no self intersection for any discrete ring occurs. As such, this layer is associated with a single start point, and a single end point. In Figure 5, we see a self intersection occur near $x_3 = -c_3$. In this case, a single path must be split or branched based on the p points of intersection $u_{i,p}^*$, where $u_{i,p}^*$ is defined using the condition presented in Equation (6). The resultant branched paths are described by

$$\begin{aligned} x_1(u_{i,j}, v_{i,j}) &= c_1 \cos(u_{i,j}) \sin(v_{i,j}) \\ x_2(u_{i,j}, v_{i,j}) &= c_2 \sin(u_{i,j}) \sin(v_{i,j}). \end{aligned} \quad (7)$$

In the case of Figure 6, a single intersection occurs, and the subsequent split paths are defined by first cropping the remaining two surfaces. Once cropped, the two surfaces are filled to define the branches using steps matching those of the original decomposition process with the only exception being the definition of the first ring. In this case, $x_1(u_{0,j}, v_{0,j})$, $x_2(u_{0,j}, v_{0,j})$, and $x_3(u_{0,j}, v_{0,j})$ are defined along the cropped edge of the surface. This basic procedure of defining the initial ring along an edge further applies to discretizing open surfaces.

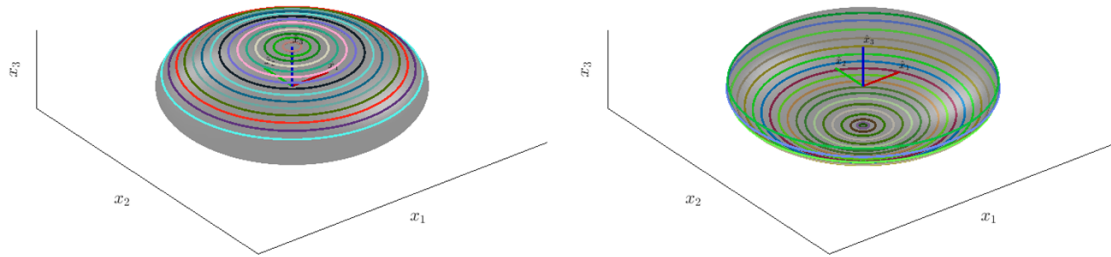


Figure 5. Ellipsoid where $c_1 = c_2$ with overlaid concentric paths propagated from $x_3 = c_3$. Paths on the top of the ellipsoid are shown on the left, and paths on the bottom are shown on the right.

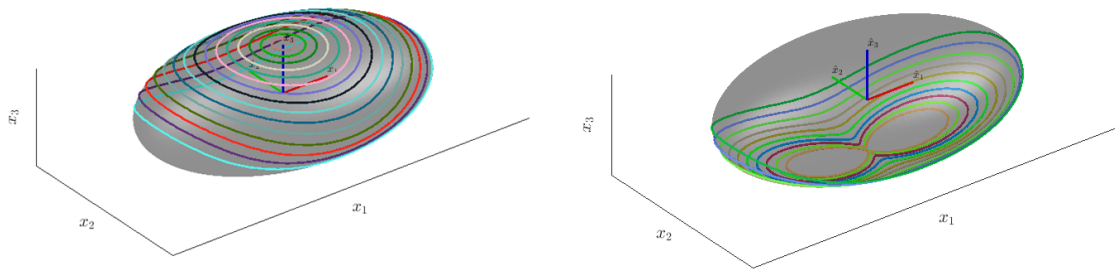


Figure 6. Ellipsoid where $c_1 \neq c_2$ with overlaid concentric paths propagated from $x_3 = c_3$. Paths on the top of the ellipsoid are shown on the left, and paths on the bottom are shown on the right.

With the entire layer decomposed into rings, one or more paths can be created to cover the surface. To do so, we first parametrize the system over $w \in [0, 1]$, defining the parametrized coordinates of ring i using the vector $\vec{x}_i(w)$ defined in Equation (8).

$$\vec{x}_i(w) = \begin{pmatrix} x_1(u, v_i; w) \\ x_2(u, v_i; w) \\ x_3(u, v_i; w) \end{pmatrix} \quad (8)$$

Using this parametrization, rings are “cut” subject to the deposition constraint proposed in Equation (5) such that

$$|\vec{x}_i(0) - \vec{x}_i(1)| = 2r. \quad (9)$$

Doing so further restricts the bounds on u on a ring-by-ring basis. We define u_i for each cut ring such that $u_i(w) \subset [0, 2\pi)$. To maintain aligned cuts, selection of $u_i(0)$ for $i > 0$ is defined such that

$$|\vec{x}_i(0) - \vec{x}_{i-1}(0)| = |\vec{x}_i(1) - \vec{x}_{i-1}(1)|. \quad (10)$$

Once cut, rings must be smoothly connected or “stitched” to create a contiguous path. Assuming small r , stitches are defined by refining the end conditions of each ring. To do so, we introduce offset conditions for w for each ring and end point such that

$$|\vec{x}_i(\Delta w_i(0)) - \vec{x}_i(0)| = r \quad (11)$$

$$|\vec{x}_i(\Delta w_i(1)) - \vec{x}_i(1)| = r \quad (12)$$

where $\Delta w_i(0)$ defines an offset from $\vec{x}_i(0)$, and $\Delta w_i(1)$ defines an offset from $\vec{x}_i(1)$. For small r , we note that Euclidean norm is approximately equal to the distance along the surface. This allows us to define a stitch between each ring using an arc of constant curvature (approximately equal to r) from $\vec{x}_{i-1}(\Delta w_{i-1}(0))$ to $\vec{x}_i(\Delta w_i(0))$ and from $\vec{x}_{i-1}(\Delta w_{i-1}(1))$ to $\vec{x}_i(\Delta w_i(1))$ for all $i \in \{1, 2, \dots, i_{max}\}$.

Once rings are stitched, a wave function with bounds at 0 and 1 defined over $\xi \in [0, i_{max} + 1)$ (e.g., Equation (13)) is used to define a contiguous path.

$$w(\xi) = \frac{1}{2} \sin\left(\pi\xi - \frac{\pi}{2}\right) + \frac{1}{2} \quad (13)$$

Defining $w(\xi)$ per Equation (13) allows the deposition path to be defined

$$\vec{x}(\xi) = \vec{x}_{[\xi]}(w; \xi). \quad (14)$$

For this application, paths are extended from a three dimensional position, to a 5-DOF pose (position in three dimensions and deposition direction prescribed by two angles). This is critical when prescribing tool orientation during deposition. Intuitively, deposition must occur with the tool-head aligned with the surface normal. Using the parametrization provided in Equation (3), the surface normal is defined

$$\vec{N} = \frac{\partial \vec{x}}{\partial u} \times \frac{\partial \vec{x}}{\partial v}, \quad (15)$$

where $\vec{x} = (x_1(u, v), x_2(u, v), x_3(v))^T$ and \vec{N} defines the surface normal relative to the body-fixed coordinate frame. With a deposition path and orientation prescribed, the deposition trajectory can be defined.

4. Deposition Trajectory Generation

For this FDM inspired application, trajectories are defined by parameterizing paths in time subject to the bounds of the deposition tool-head. Assume the tool-head extrudes material at a linear rate d which is continuously variable between 0 (no material is deposited) and d_{max} (the maximum allowable rate of deposition). At any given point along the trajectory, the instantaneous speed must be bounded by d . Equation (16) defines this relationship between speed and deposition rate where $\vec{T}(t)$ defines the time-evolving tangent to the path and instantaneous speed is defined as the Euclidean norm of the tangent.

$$\left| \vec{T}(t) \right| \leq d_{max} \quad (16)$$

Parameterizing the path with respect to arc length simplifies the derivation of the trajectory noting that, by definition

$$\left| \vec{T}(s) \right| = \left| \frac{d\vec{x}(s)}{ds} \right| = 1 \quad (17)$$

where $s \in [0, 1]$. This enables a constant deposition rate of \mathbf{d}^* defined within the bounds of d to be applied. Given the path parametrized by arc length, the function $s(t)$ can be defined noting Equation (18).

$$\left| \vec{T}(t) \right| = \left| \frac{\partial \vec{x}(s)}{\partial s} \frac{\partial s(t)}{\partial t} \right| = \mathbf{d}^*. \quad (18)$$

Noting that $\frac{\partial s(t)}{\partial t}$ is a scalar and $s(t)$ is strictly increasing, $s(t)$ can be defined

$$s(t) = \int_0^t \mathbf{d}^* d\tau = \mathbf{d}^* t. \quad (19)$$

Build-object and tool-head trajectories are derived from the deposition trajectory using a model-based approach. Assuming the redundancy present in the proposed dual manipulator system, there is the potential for multiple sets of coordinated manipulator trajectories that result in the same deposition trajectory. This allows candidate sets to be evaluated in simulation to check for issues related to interference, collision, and joint velocities/accelerations exceeding the physical capabilities of the hardware. This redundancy also makes it possible to impose additional constraints on the system to adhere to desired criteria (e.g., actively reorienting the deposition direction relative to gravity).

The primary drawback to this level of redundancy is the extensive search space associated with two coordinated manipulators. For the purposes of this work, the search space is reduced by assuming a trajectory for the build-object, and deriving an interference and collision-free trajectory for the tool-head. This is accomplished using a variety of available tools (e.g., MoveIt! [17]). While effective for this application, this approach may be improved using methods from existing research [18,19], however this is outside of the scope of this work.

5. Testbed Design

5.1. Hardware Overview

An asymmetric set of two independent six degree-of-freedom (6-DOF) manipulators (UR5 and UR10, Universal Robots A/S, Odense, Denmark), a single gripper (2-Finger Adaptive Robot Gripper, Robotiq Inc., Lévis, QC, Canada), a single tool-head (3Doodler v1.0, WobbleWorks, LLC., Somerville, MA, USA), and a 14 camera motion capture system (OptiTrack Prime 41, NaturalPoint Inc., Corvallis, OR, USA) comprise the system testbed. The asymmetry in manipulator geometry enables a large shared workspace in x , y , z , and \hat{z} tool coordinates. Here, x , y , and z denote the tool position, and \hat{z} denotes the z -direction of the tool frame. Figure 7 provides an annotated view of the system.

Control of the testbed consists of four key items (1) Interfacing and controlling the Universal Robot hardware to execute a coordinated set of smooth, prescribed trajectories; (2) Interfacing the Robotiq gripper to reliably respond to a known command set; (3) Creating an electronic interface with the 3Doodler capable of responding to a known command set to control material feed rate; and (4) Registering and tracking the build object and tool-head using the motion capture system. The following sections will address items (1) and (4) in detail.

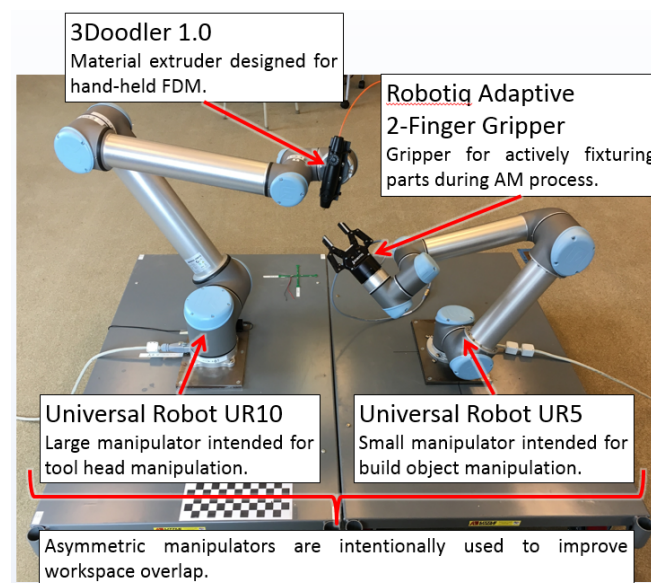


Figure 7. System testbed highlighting key components.

5.2. Controller Design

Interfacing and controlling the Universal Robot hardware to execute a coordinated set of smooth, prescribed trajectories requires the development of an on-board intermediate control algorithm. A script implementing an intermediate controller was developed to run directly on the UR operating system. This script leverages a modified PID approach wherein desired discrete set of joint positions ($\vec{q}_d(t_i)$) and velocities ($\dot{\vec{q}}_d(t_i)$) are sent to the manipulator, and the controller generates a continuous commanded joint velocity ($\dot{\vec{q}}(t)$) for the manipulator. The current implementation utilizes

a proportional controller, $k_p > 0$, where discrete time steps are denoted using t_i , and continuous terms (available as direct feedback on-board the UR operating system) are denoted as functions of t .

$$\dot{\vec{q}}(t) = k_p (\vec{q}_d(t_i) - \vec{q}(t)) \quad (20)$$

To interface each Universal Robot, a MATLAB class [20] was created wrapping existing functionality from the available URX Python Library [21]. This class develops a custom command structure for sending and receiving information to/from the control script. This allows the UR to respond to a continuous stream of joint position/velocity waypoints in a smooth manner. Commands are sent to each manipulator via a TCP/IP connection from a PC running a single instance of MATLAB. Time-stamped waypoints are calculated off-line and sent to each manipulator at a known interval. This enables coordination driven by the clock of the host PC.

5.3. System Kinematics

As was introduced in Figure 1, successful operation of this dual manipulator testbed requires the measurement and estimation of numerous transformations between coordinate frames in space. Frames are initially assigned using available measurements from the motion capture system and joint measurements from each Universal Robot. The motion capture system provides position and orientation (also referred to as pose) measurements of rigid configurations of reflective markers relative to a static world frame. Each Universal Robot provides the pose of their end-effector relative to their respective base frame. This introduces Frame w , Frame b_1 , Frame b_2 , Frame E_1 , and Frame E_2 defined in Table 2; where the UR5 provides $H_{E_1}^{b_1}$ (the pose, represented as a rigid body transformation, of Frame E_1 relative to Frame b_1), and the UR10 provides $H_{E_2}^{b_2}$.

Table 2. Coordinate frame definitions for the dual manipulator testbed.

Label	Description
Frame w	Motion Capture World Frame
Frame b_1	UR5 Base Frame
Frame b_2	UR10 Base Frame
Frame E_1	UR5 End-effector Frame
Frame E_2	UR10 End-effector Frame
Frame m_1	Marker Frame rigidly fixed relative to Frame b_1
Frame m_2	Marker Frame rigidly fixed relative to Frame b_2
Frame T_1	The body-fixed coordinate frame of the build-object (rigidly fixed relative to Frame E_1)
Frame T_2	The tool-head coordinate frame with \hat{z} aligned with the material feed direction and offset from the nozzle per manufacturer recommendations (rigidly fixed relative to Frame E_1)

Noting that no pose information between the manipulators is known, we fix a rigid set of reflective markers relative to the base of each manipulator. This introduces Frame m_1 and Frame m_2 (Table 2) where the motion capture provides $H_{m_1}^w$ and $H_{m_2}^w$. Section 5.4 addresses the experimental estimation of $\mathbf{H}_{m_1}^{b_1}$ and $\mathbf{H}_{m_2}^{b_2}$.

To account for the build-object and tool-head, we introduce Frame T_1 and Frame T_2 (Table 2) where CAD models of the gripper and build-object provide an initial estimate of $\mathbf{H}_{T_1}^{E_1}$, and a CAD model of the tool-head provides an initial estimate of $\mathbf{H}_{T_2}^{E_2}$. Section 5.4 addresses refinement and validation of $\mathbf{H}_{T_1}^{E_1}$ and $\mathbf{H}_{T_2}^{E_2}$. A simulation of the testbed with labeled frame assignments is provided in Figure 8.

These transformations are combined to provide $H_{T_2}^{T_1}$, the rigid body transformation relating the tool-head to the body-fixed frame of the build-object using

$$H_{T_2}^{T_1} = \mathbf{H}_{E_1}^{T_1} H_{b_1}^{E_1} \mathbf{H}_{m_1}^{b_1} H_W^{m_1} H_{m_2}^W \mathbf{H}_{b_2}^{m_2} H_{E_2}^{b_2} \mathbf{H}_{T_2}^{E_2}. \quad (21)$$

Noting the derivations in Sections 3 and 4, Frame T_1 is analogous to the body-fixed frame of each surface, path, and trajectory. Therefore, the evolution of $H_{T_2}^{T_1}$ with time is directly prescribed by the trajectory.

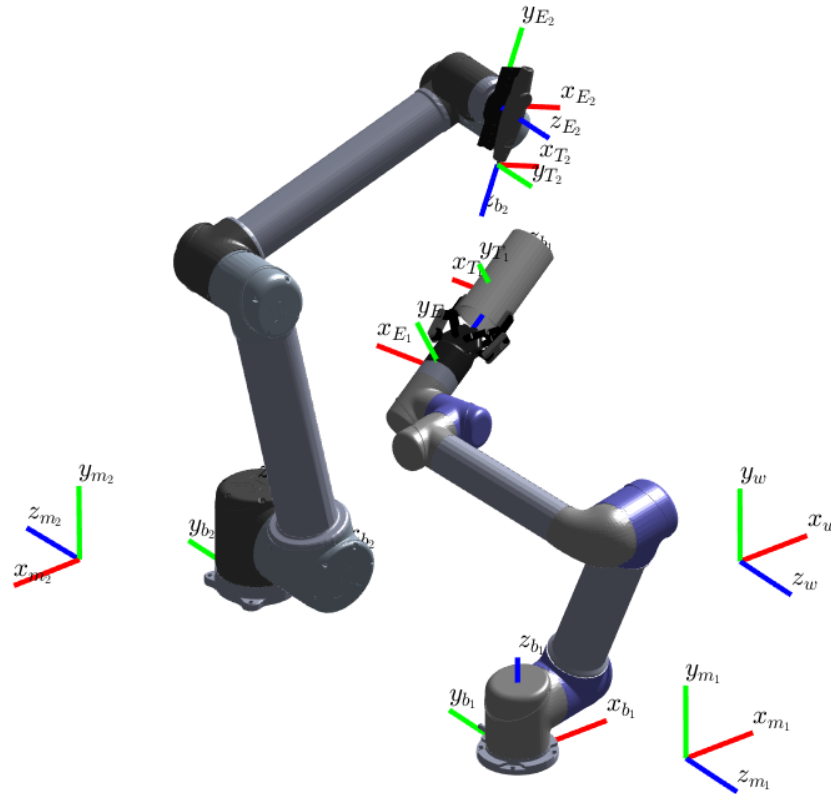


Figure 8. Simulation of system testbed highlighting frame definitions.

5.4. Calibration

System calibration is performed by first creating calibration rigid bodies for each manipulator. Noting the manufacturer's assignment of Frame E_1 for the UR5, and Frame E_2 for the UR10, two calibration objects are designed to precisely place a set of reflective markers at known locations relative to each. A rendering of the UR5 rigid body is shown in Figure 9, and the fabricated rigid bodies for both the UR5 and UR10 are shown in Figure 10.

Using [22], $H_{E_1}^W$ and $H_{E_2}^W$ are estimated from the measured marker locations returned by the motion capture system. Using these measurements, $\mathbf{H}_{m_1}^{b_1}$ and $\mathbf{H}_{m_2}^{b_2}$ are estimated

$$\mathbf{H}_{m_i}^{b_i} = H_{E_i}^{b_i} H_W^{E_i} H_{m_i}^W \quad \forall i \in \{1, 2\} \quad (22)$$

where $H_{E_i}^{b_i}$ is measured by the respective Universal Robot, $H_W^{E_i}$ and $H_{m_i}^W$ are measured using the motion capture, and $H_W^{E_i} = \left(H_{E_i}^W\right)^{-1}$. Given the inherent uncertainty associated with experimentally measured parameters, we refine the estimate of $\mathbf{H}_{m_i}^{b_i}$ for each manipulator by collecting a large number of samples over the manipulator workspace and calculating the mean of the resultant set of $\mathbf{H}_{m_i}^{b_i}$ using [23].

Estimates of $\mathbf{H}_{T_1}^{E_1}$ and $\mathbf{H}_{T_2}^{E_2}$ can be refined using techniques commonly applied to computer assisted surgical systems and computer vision. Using a precision machined probe [24] with known correspondence between the tip position and body-fixed frame, points along the outer surface of the build-object can be digitized relative to Frame W . Using these points and associated CAD models of

the build-object and tool-head, $\mathbf{H}_{T_1}^{E_1}$ and $\mathbf{H}_{T_2}^{E_2}$ can be refined using [25]. Further refinement of $\mathbf{H}_{T_2}^{E_2}$ can be performed by precisely estimating nozzle tip position using a pivot calibration [26].

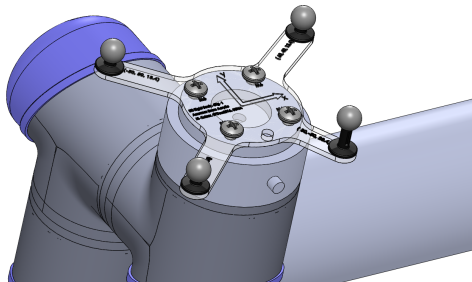


Figure 9. CAD model of the calibration rigid body designed for the UR5 manipulator.



Figure 10. Fabricated calibration rigid bodies for the UR5 (left) and UR10 (right) manipulators.

6. Results

Experimental validation was conducted by evaluating the techniques discussed in this work applied to a single layer of deposition onto a 75 mm long cylindrical build object matching the outside diameter of standard 3 in (76.2 mm) schedule 40 PVC pipe with an outside diameter of 88.9 mm. Ring spacing was defined assuming that the deposition radius of r is equal to the 1.0 mm (one half of the extrusion nozzle diameter increased by a margin of 0.5 mm). Note that, in practice, the value for r should be defined experimentally and is typically larger than the extrusion nozzle diameter. A deposition path was derived using the methods described in Section 3, and a trajectory was derived using the methods described in Section 4 with $d^* = 40$ mm/s. Figure 11 (left) shows the cylindrical layer decomposed into cut rings, and Figure 11 (right) shows the stitched rings used to generate the path and trajectory.

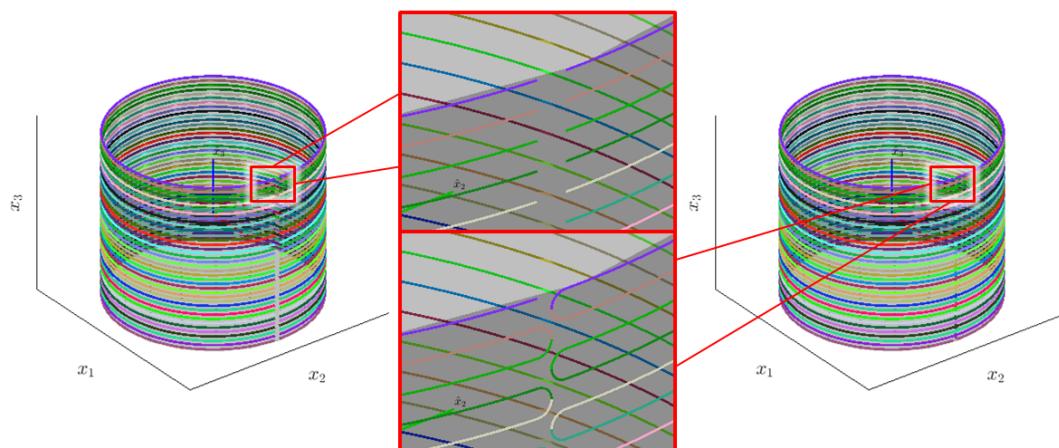


Figure 11. Cylindrical surface decomposed into cut rings (left) and stitched rings used to generate the deposition path (right).

6.1. Calibration Results

System calibration was conducted using the calibration rigid bodies described in Section 5.4. A total of 28 samples were taken from each manipulator over a discrete set of joint configurations defined over the outside of the workspace. For each arm, the mean transformation relating Frame m_i to b_i was calculated. Calibration results are analyzed using the RMS error between the fixed marker locations on the base of each manipulator measured by the motion capture, and the marker locations estimated using $H_{m_i}^W$ defined

$$H_{m_i}^W = H_{E_i}^W H_{b_i}^{E_i} \mathbf{H}_{m_i}^{b_i}. \quad (23)$$

Results from the UR5 calibration are presented in Figure 12 (left), and results from the UR10 calibration are presented in Figure 12 (right).

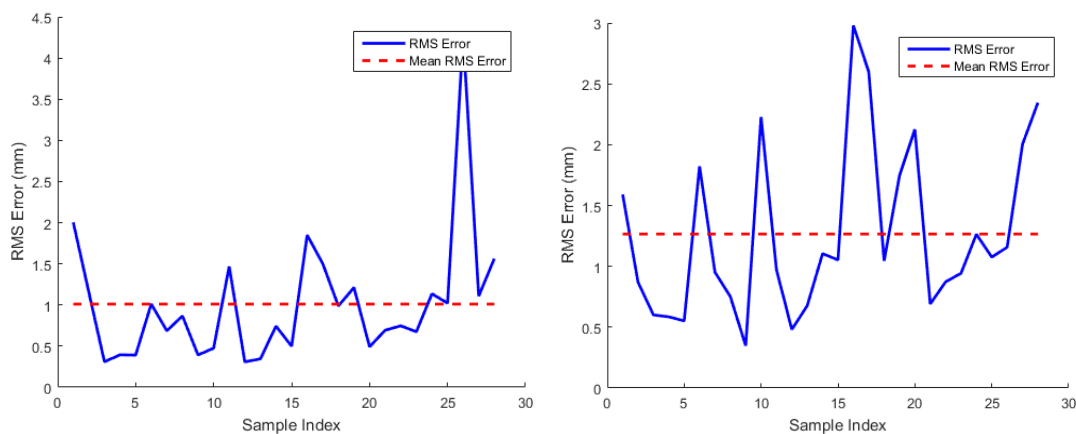


Figure 12. RMS error calculated between measured marker locations and marker location estimates calculated with $\mathbf{H}_{m_1}^{b_1}$ (left) and $\mathbf{H}_{m_2}^{b_2}$ (right).

6.2. Controller Results

The intermediate controller was analyzed by comparing the control signal sent to each robot to the actual end-effector position while executing the deposition trajectory. Results from the UR5 are presented in Figure 13 (left), and results from the UR10 are presented in Figure 13 (right).

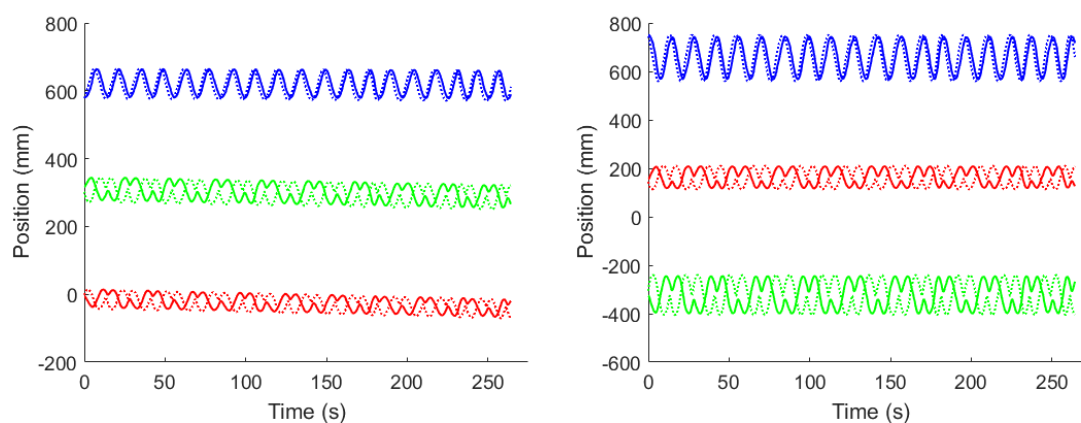


Figure 13. Comparison between actual end-effector position and commanded end-effector position for the UR5 (left) and UR10 (right). Actual position is represented using a solid line, and command position is represented using a dashed line. x , y , and z positions are differentiated using red, green, and blue respectively.

6.3. System Performance

The overall performance of the system was analyzed by comparing the commanded and measured deposition trajectories estimated using $H_{T_2}^{T_1}$. Comparison results for the position in the body-fixed x -direction are presented in Figure 14, the body-fixed y -direction in Figure 15, and the body-fixed z -direction in Figure 16.

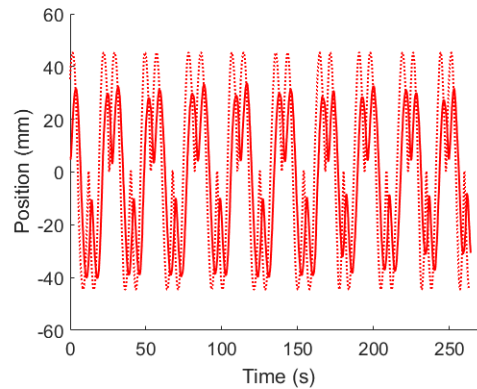


Figure 14. Comparison between the x -position of the actual deposition trajectory and the commanded deposition trajectory. Actual position is represented using a solid line, and command position is represented using a dashed line.

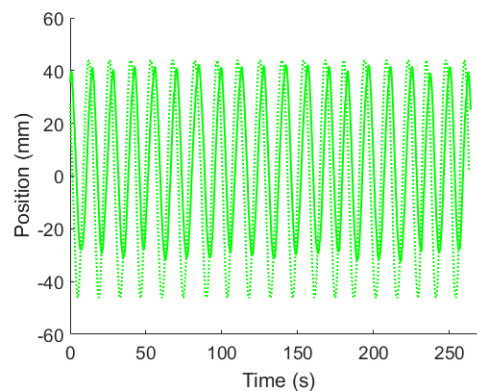


Figure 15. Comparison between the y -position of the actual deposition trajectory and the commanded deposition trajectory. Actual position is represented using a solid line, and command position is represented using a dashed line.

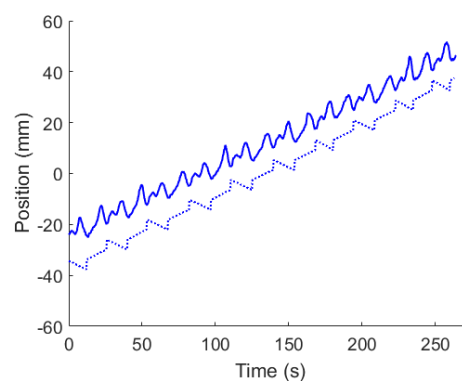


Figure 16. Comparison between the z -position of the actual deposition trajectory and the commanded deposition trajectory. Actual position is represented using a solid line, and command position is represented using a dashed line.

7. Discussion

System calibration was quantified by calculating mean RMS error associated with the difference between measured and estimated marker positions. This RMS error is a measure of accuracy for $\mathbf{H}_{m_i}^{b_i}$ that accounts for errors in both position and orientation associated with the estimated transformation. Experiments showed an RMS error for $\mathbf{H}_{m_1}^{b_1}$ of 1.01 mm, and an RMS error for $\mathbf{H}_{m_2}^{b_2}$ of 1.27 mm. These errors are reasonable when considering the published worst case performance specifications from both Universal Robots and NaturalPoint; however this error must be reduced before actual material deposition can occur. Error reduction using the current and proposed system tools discussed in Section 5.4 is the subject of ongoing work. An additional solution for error reduction using a shared, precision machined base for both manipulators is under consideration, however this may limit system versatility.

Experiments showed that, for the cyclic trajectories used in this paper, the end-effector tracking errors reached a steady state amplitude of approximately 20 mm and phase lag of π radians. However, both manipulators were found to have the same tracking error characteristics, so the relative trajectories remained within spatial tolerances of the tool-head. Iteration of the control design including integral and derivative terms to improve tracking performance is the subject of ongoing work.

Comparisons of the commanded and measured trajectories show discrepancies that reach and exceed 10 mm in position data, however these results are expected given the analysis of system calibration and control. Given the RMS error measurements associated with $\mathbf{H}_{m_1}^{b_1}$ of 1.01 mm, and an RMS error for $\mathbf{H}_{m_2}^{b_2}$ of 1.27 mm; these discrepancies are explained primarily by an orientation misalignment associated with the estimated transformations relating the marker frame to the base frame for each robot. Refining system calibration using the methods described in Section 5.4 will further reduce this error. Analysis of the published performance capabilities for the UR manipulators and motion capture system suggest that this error can be reduced to better than ± 1.0 mm. Performance can be further improved using a shared, precision machined base for both manipulators; eliminating tracking errors associated with the motion capture system. As mentioned previously, this approach may limit system versatility. Methods to reduce this error using the tools discussed in Section 5.4 are the subject of ongoing work.

Additional analysis of the comparisons of the commanded and measured trajectory results also suggest that the selection of \mathbf{d}^* may have an effect on deposition tracking performance. While the prescribed trajectory was within the performance limitations of the system, a reduced value of \mathbf{d}^* may provide improved tracking accuracy. Further investigation into the relationship between the selection of \mathbf{d}^* and tracking performance is the subject of ongoing work.

8. Conclusions

We have presented a systematic approach for multilayer conformal additive manufacturing inspired by the work presented in [5]. This work included a new approach to generate appropriately spaced paths to fill the surface of three dimensional layers. Paths were used to derive time evolving trajectories using arc length parametrization and the extrusion rate of the tool-head. The application of these methods to a relevant hardware system was discussed, and topics including control, characterization, and calibration were addressed. Results from this work suggest the feasibility of this approach in a relevant context; however future work is required to refine system performance.

Acknowledgments: This work was supported by Office of Naval Research FY16 Grant No. N0001416WX00796. The authors thank Greg Chirikjian, Josh Davis, and Jin Seob Kim for their contributions to the foundation of this work, and ENS Kevin Strotz for his contributions to the Universal Robots MATLAB Toolbox as a TAD Ensign during the summer of 2016.

Author Contributions: Kutzer M.D.M. developed path and trajectory generation methods. DeVries L.D. defined and evaluated intermediate controller for the manipulator. Kutzer M.D.M. designed experiments; Kutzer M.D.M. and DeVries L.D. performed experiments and analyzed data.

Conflicts of Interest: The authors declare no conflict of interest.

References

1. Scheck, C. Introduction to Additive Manufacturing (AM 101). Available online: http://www.nsrp.org/wp-content/uploads/2016/01/Presentation-Joint_120815-AM_101-NSWCCD.pdf (accessed on 19 May 2016).
2. Frazier, W.E. Direct digital manufacturing of metallic components: Vision and roadmap. In Proceedings of the 21st Annual International Solid Freeform Fabrication Symposium, Austin, TX, USA, 9–11 August 2010; pp. 717–732.
3. Goehrke, S. NAVAIR Has Big Plans for Additive Manufacturing. Available online: <https://3dprint.com/58698/navair-additive-manufacturing/> (accessed on 25 May 2016).
4. Harper, J. Military 3D Printing Projects Face Challenges. *Natl. Def. Ind. Assoc. Bus. Technol. Mag.* **2015**, *100*, 24.
5. Davis, J.D.; Kutzer, M.D.; Chirikjian, G.S. Algorithms for Multilayer Conformal Additive Manufacturing. *J. Comput. Inf. Sci. Eng.* **2016**, *16*, 021003.
6. Gibson, I.; Rosen, D.W.; Stucker, B. *Additive Manufacturing Technologies: Rapid Prototyping to Direct Digital Manufacturing*; Springer: New York, NY, USA, 2010.
7. Radtke, D.; Zeitner, U.D. Laser-lithography on non-planar surfaces. *Opt. Express* **2007**, *15*, 1167–1174.
8. Xie, Y.; Lu, Z.; Jingli, F.L.; Yongjun, Z.; Zhao, J.; Weng, Z. Lithographic fabrication of large diffractive optical elements on a concave lens surface. *Opt. Express* **2002**, *10*, 1043–1047.
9. Adams, J.J.; Duoss, E.B.; Malkowski, T.F.; Motala, M.J.; Ahn, B.Y.; Nuzzo, R.G.; Bernhard, J.T.; Lewis, J.A. Conformal Printing of Electrically Small Antennas on Three-Dimensional Surfaces. *Adv. Mater.* **2011**, *23*, 1335–1340.
10. Paulsen, J.; Renn, M.; Christenson, K.; Plourde, R. Printing conformal electronics on 3D structures with Aerosol Jet technology. In Proceedings of the Future of Instrumentation International Workshop (FIIW), Gatlinburg, TN, USA, 8–9 October 2012; pp. 1–4.
11. Directed Energy Deposition. Available online: <http://www.lboro.ac.uk/research/amrg/about/the7categoriesofadditivemanufacturing/directedenergydeposition/> (accessed on 25 May 2016).
12. Bertoldi, M.; Yardimci, M.; Pistor, C.; Guceri, S. Domain decomposition and space filling curves in toolpath planning and generation. In Proceedings of the 1998 Solid Freeform Fabrication Symposium, Austin, TX, USA, 11–13 August 1998; pp. 267–274.
13. Yang, Y.; Fuh, J.Y.; Loh, H.T. An efficient scanning pattern for layered manufacturing processes. In Proceedings of the IEEE International Conference on Robotics and Automation (2001 ICRA), Seoul, Korea, 21–26 May 2001; Volume 2, pp. 1340–1345.
14. Sadourny, R. Conservative finite-difference approximations of the primitive equations on quasi-uniform spherical grids. *Mon. Weather Rev.* **1972**, *100*, 136–144.
15. Stratasys Ltd. Optimizing Seam Location. Available online: http://usglobalimages.stratasys.com/Main/Files/Best%20Practices_BP/BP_OptimizingSeamLocation.pdf?v=635817995301407599 (accessed on 25 May 2016).
16. Hopkins, P.E.; Holzwarth, D.J. Seam Concealment for Three-Dimensional Models. U.S. Patent 8,974,715, 10 March 2015.
17. Sucas, I.A.; Chitta, S. MoveIt! Available online: <http://moveit.ros.org> (accessed on 17 May 2017).
18. Latombe, J.C. *Robot Motion Planning*; Kluwer Academic Publishers: Norwell, MA, USA, 1991.
19. Ata, A.A. Optimal trajectory planning of manipulators: A review. *J. Eng. Sci. Technol.* **2007**, *2*, 32–54.
20. Kutzer, M. MATLAB Toolbox for UR Manipulators. Available online: https://www.usna.edu/Users/weapsys/kutzer/_Code-Development/UR_Toolbox.php (accessed on 22 May 2017).
21. Roulet-Dubonnet, O. Python Library to Control a Robot from “Universal Robots”. Available online: <https://github.com/SintefRaufossManufacturing/python-urx> (accessed on 22 May 2017).
22. Eggert, D.W.; Lorusso, A.; Fisher, R.B. Estimating 3-D rigid body transformations: A comparison of four major algorithms. *Mach. Vis. Appl.* **1997**, *9*, 272–290.
23. Long, A.W.; Wolfe, K.C.; Mashner, M.J.; Chirikjian, G.S. The banana distribution is Gaussian: A localization study with exponential coordinates. In *Robotics: Science and Systems VIII*; MIT Press: Cambridge, MA, USA 2013; pp. 265–272.
24. Chen, E.; Sati, M.; Croitoru, H.; Tate, P.; Fu, L. Computer-Assisted Surgical Positioning Method and System. U.S. Patent 10/467,445, 6 May 2004.

25. Mitra, N.J.; Gelfand, N.; Pottmann, H.; Guibas, L. Registration of point cloud data from a geometric optimization perspective. In Proceedings of the 2004 Eurographics/ACM SIGGRAPH Symposium on Geometry Processing, Nice, France, 8–10 July 2004; pp. 22–31.
26. Otake, Y.; Armand, M.; Sadowsky, O.; Armiger, R.; Kutzer, M.; Mears, S.; Kazanzides, P.; Taylor, R. An image-guided femoroplasty system: Development and initial cadaver studies. *Proc. SPIE* **2010**, *7625*, 76250P.



© 2017 by the authors. Licensee MDPI, Basel, Switzerland. This article is an open access article distributed under the terms and conditions of the Creative Commons Attribution (CC BY) license (<http://creativecommons.org/licenses/by/4.0/>).